CORONAVIRUS

Versatile and multivalent nanobodies efficiently neutralize SARS-CoV-2

Yufei Xiang[1], Sham Nambulli[2,3]*, Zhengyun Xiao[1]*, Heng Liu[4]*, Zhe Sang[1,5], W. Paul Duprex[2,3], Dina Schneidman-Duhovny[6]†, Cheng Zhang[4]†, Yi Shi[1,5]†

Cost-effective, efficacious therapeutics are urgently needed to combat the COVID-19 pandemic. In this study, we used camelid immunization and proteomics to identify a large repertoire of highly potent neutralizing nanobodies (Nbs) to the severe acute respiratory syndrome coronavirus 2 (SARS-CoV-2) spike protein receptor binding domain (RBD). We discovered Nbs with picomolar to femtomolar affinities that inhibit viral infection at concentrations below the nanograms-per-milliliter level, and we determined a structure of one of the most potent Nbs in complex with the RBD. Structural proteomics and integrative modeling revealed multiple distinct and nonoverlapping epitopes and indicated an array of potential neutralization mechanisms. We bioengineered multivalent Nb constructs that achieved ultrahigh neutralization potency (half-maximal inhibitory concentration as low as 0.058 ng/ml) and may prevent mutational escape. These thermostable Nbs can be rapidly produced in bulk from microbes and resist lyophilization and aerosolization.

Globally a novel, highly transmissible coronavirus—severe acute respiratory syndrome coronavirus 2 (SARS-CoV-2) (*1*, *2*)—has infected more than 30 million people and has claimed almost 1 million lives, with the numbers still rising as of September 2020. Despite preventive measures, such as quarantines and lockdowns that help curb viral transmission, the virus rebounds after social restrictions are lifted. Safe and effective therapeutics and vaccines remain urgently needed.

Like other zoonotic coronaviruses, SARS-CoV-2 expresses a surface spike (S) glycoprotein, which consists of S1 and S2 subunits that form a homotrimeric viral spike to interact with host cells. The interaction is mediated by the S1 receptor binding domain (RBD), which binds the peptidase domain of human angiotensin-converting enzyme 2 (hACE2) as a host receptor (*3*). Structural studies have revealed different conformations of the spike (*4*, *5*). In the prefusion stage, the RBD switches between a closed conformation and an open conformation for hACE2 interaction. In the postfusion stage, the S2 undergoes a substantial conformational change to trigger host membrane fusion (*6*). Investigations of sera from COVID-19 convalescent individuals have led to the identification of potent neutralizing antibodies (NAbs) that primarily target the RBD but also non-RBD epitopes (*7*–*13*). High-quality NAbs may overcome the risks of Fc-associated antibody-dependent enhancement and are promising therapeutic candidates (*14*, *15*).

V_HH antibodies, or nanobodies (Nbs), are minimal, monomeric antigen binding domains derived from camelid single-chain antibodies (*16*). Unlike immunoglobulin G (IgG) antibodies, Nbs are small (~15 kDa), highly soluble and stable, readily bioengineered into bi- or multivalent forms, and amenable to low-cost, efficient microbial production. Owing to their robust physicochemical properties, Nbs can be administered by inhalation, which makes them appealing therapeutic agents for treatment of respiratory viruses (*17*, *18*). Recently, several SARS-CoV-2 neutralizing Nbs have been identified through the screening of SARS-CoV or Middle East respiratory syndrome (MERS) cross-reacting Nbs or the use of synthetic Nb libraries for RBD binding. However, these synthetic Nbs generally neutralize the virus at or below microgram-per-milliliter concentrations (*12*, *19*–*22*) and thus are hundreds of times less potent than the most effective NAbs, likely due to monovalency and/or lack of affinity maturation (*23*, *24*). The development of highly potent anti–SARS-CoV-2 Nbs may provide a means for versatile, cost-effective prophylaxis, therapeutics, and point-of-care diagnosis.

To produce high-quality SARS-CoV-2 neutralizing Nbs, we immunized a llama with the recombinant RBD. Compared with the preimmunized serum sample, the postimmunized serum showed potent and specific serologic activities toward RBD binding with a titer of 1.75×10^6 (fig. S1A). The serum efficiently neutralized the pseudotyped SARS-CoV-2 at a half-maximal neutralization titer (NT_{50}) of ~310,000 (fig. S1B), orders of magnitude higher than that of the convalescent sera obtained from recovered COVID-19 patients (*7*, *8*). To further characterize these activities, we separated the single-chain V_HH antibodies from the IgGs. We confirmed that the single-chain antibodies achieve specific, high-affinity binding to the RBD and possess subnanometer half-maximal inhibitory concentration (IC_{50} = 509 pM) against the pseudotyped virus (fig. S1C).

We identified thousands of high-affinity V_HH Nbs from the RBD-immunized llama serum by using a robust proteomic strategy that we recently developed (*25*) (fig. S2A). This repertoire includes ~350 distinct CDR3s (CDRs, complementarity-determining regions). For *Escherichia coli* expression, we selected 109 highly diverse Nb sequences from the repertoire with distinct CDR3s to cover various biophysical, structural, and potentially different antiviral properties. Ninety-four Nbs were purified and tested for RBD binding by enzyme-linked immunosorbent assay (ELISA), from which we confirmed 71 RBD-specific binders (fig. S2, B and C, and tables S1 and S4). Of these RBD-specific binders, 49 Nbs presented high solubility and high affinity (ELISA IC_{50} below 30 nM; Fig. 1A) and were promising candidates for functional characterizations. We used a SARS-CoV-2–green fluorescent protein (GFP) pseudovirus neutralization assay to screen and characterize the antiviral activities of these high-affinity Nbs. Of the tested Nbs, 94% neutralize the pseudotype virus below 3 μM (Fig. 1B), and 90% neutralize below 500 nM. Only 20 to 40% of the high-affinity RBD-specific monoclonal antibodies identified from patient sera have been reported to possess comparable potency (*7*, *8*). More than three-quarters (76%) of the Nbs efficiently neutralized the pseudovirus below 50 nM, and 6% had neutralization activities below 0.5 nM. We selected the 18 most potent Nbs on the basis of the pseudovirus GFP reporter screen and measured their potency accurately using the pseudovirus-luciferase reporter assay. Finally, we used the plaque reduction neutralization test (PRNT) assay (*26*) to evaluate the potential of 14 Nbs to neutralize the SARS-CoV-2 Munich strain. All of the Nbs reached 100% neutralization and neutralized the virus in a dose-dependent manner. The IC_{50} values range from single-digit nanograms-per-milliliter amounts to below the nanograms-per-milliliter level. Of the most potent Nbs, three of them (89, 20, and 21) showed neutralization of 2.1 ng/ml (0.133 nM), 1.6 ng/ml (0.102 nM), and 0.7 ng/ml (0.045 nM), respectively, in the pseudovirus assay (Fig. 1C) and 0.154, 0.048, and 0.022 nM, respectively, in the SARS-CoV-2 assay (Fig. 1, D and E). Overall, there was an excellent

[1]Department of Cell Biology, University of Pittsburgh, Pittsburgh, PA, USA. [2]Center for Vaccine Research, University of Pittsburgh, Pittsburgh, PA, USA. [3]Department of Microbiology and Molecular Genetics, University of Pittsburgh, Pittsburgh, PA, USA. [4]Department of Pharmacology and Chemical Biology, University of Pittsburgh, Pittsburgh, PA, USA. [5]University of Pittsburgh–Carnegie Mellon University Program in Computational Biology, Pittsburgh, PA, USA. [6]School of Computer Science and Engineering, Institute of Life Sciences, The Hebrew University of Jerusalem, Jerusalem, Israel.
*These authors contributed equally to this work.
†Corresponding author. Email: dina.schneidman@mail.huji.ac.il (D.S.-D.); chengzh@pitt.edu (C.Z.); yi.shi@pitt.edu (Y.S.)

correlation between the two neutralization assays (R^2 = 0.92; fig. S3).

We measured the binding kinetics of Nbs 89, 20, and 21 by surface plasmon resonance (SPR) (fig. S4, A and B). Nbs 89 and 20 have affinities of 108 and 10.4 pM, respectively, and the most potent Nb21 did not show detectable dissociation from the RBD during 20 min of SPR analysis. The subpicomolar affinity of Nb21 potentially explains its unusual neutralization potency (Fig. 1F). From the *E. coli* periplasmic preparations, we determined the thermostability of Nbs 89, 20, and 21 to be 65.9°, 71.8°, and 72.8°C, respectively (fig. S4C). Finally, we tested the on-shelf stability of Nb21, which remained soluble after ~6 weeks of storage at room temperature after purification. No multimeric forms or aggregations were detected by size exclusion chromatography (SEC) (fig. S4D). Together, these results suggest that these neutralizing Nbs have valuable physicochemical properties for advanced therapeutic applications.

We employed an integrative approach by using SEC, cross-linking and mass spectrometry, and structural modeling for epitope mapping (*27*–*30*). First, we performed SEC experiments to distinguish between Nbs that share the same RBD epitope with Nb21 and those that bind to nonoverlapping epitopes. According to SEC profiles, Nbs 9, 16, 17, 20, 64, 82, 89, 99, and 107 competed with Nb21 for RBD binding (Fig. 2A and fig. S5), which indicates that their epitopes overlap substantially. By contrast, higher-mass species (from early elution volumes) corresponding to the trimeric complexes composed of Nb21, RBD, and one of the Nbs (*34*, *36*, *93*, *105*, and *95*) were evident (Fig. 2B and fig. S6, A to H). Moreover, Nb105 competed with Nbs *34* and *95*, which did not compete for RBD interaction, suggesting the presence of two distinct and nonoverlapping epitopes. Second, we used disuccinimidyl suberate (DSS) to cross-link Nb-RBD complexes, and we used mass spectrometry to identify, on average, four intermolecular cross-links for Nbs 20, *93*, *34*, *95*, and 105. The cross-links were used to map the RBD epitopes derived from the SEC data (materials and methods). Our cross-linking models identified five epitopes (I, II, III, IV, and V corresponding to Nbs 20, *93*, *34*, *95*, and 105) (Fig. 2C). The models satisfied 90% of the cross-links with an average precision of 7.8 Å (Fig. 2D and table S2). Our analysis confirmed the presence of a dominant epitope I (e.g., epitopes of Nbs 20 and 21) overlapping with the hACE2 binding site. Epitope II also co-localized with the nonconserved hACE2 binding site. Both epitopes I and II Nbs can compete with hACE2 binding to the RBD at very low concentrations in vitro (fig. S7A). Epitopes III to V colocalized with conserved sites (fig. S7, B and C). Notably, epitope I Nbs had significantly

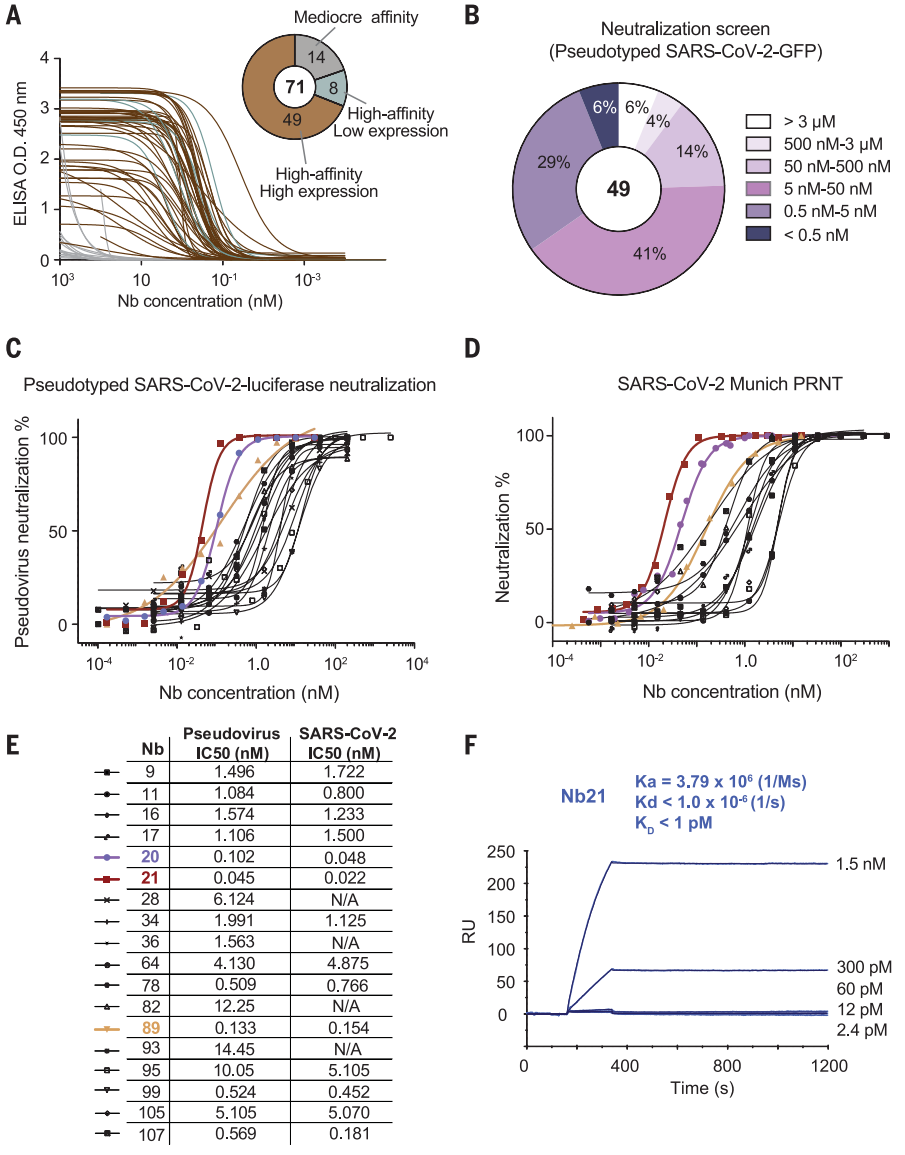

Nb	Pseudovirus IC50 (nM)	SARS-CoV-2 IC50 (nM)
9	1.496	1.722
11	1.084	0.800
16	1.574	1.233
17	1.106	1.500
20	0.102	0.048
21	0.045	0.022
28	6.124	N/A
34	1.991	1.125
36	1.563	N/A
64	4.130	4.875
78	0.509	0.766
82	12.25	N/A
89	0.133	0.154
93	14.45	N/A
95	10.05	5.105
99	0.524	0.452
105	5.105	5.070
107	0.569	0.181

Fig. 1. Production and characterizations of high-affinity RBD Nbs for SARS-CoV-2 neutralization. (**A**) Binding affinities of 71 Nbs toward the RBD, as determined by ELISA. The pie chart shows the number of Nbs according to affinity and solubility. O.D., optical density. (**B**) Screening of 49 high-affinity Nbs with high-expression level, as determined by SARS-CoV-2–GFP pseudovirus neutralization assay. n = 1 for Nbs with neutralization potency IC_{50} ≤ 50 nM; n = 2 for Nbs with neutralization potency IC_{50} > 50 nM (n indicates the number of replicates). (**C**) Neutralization potency of 18 highly potent Nbs was calculated on the basis of the pseudotyped SARS-CoV-2 neutralization assay (luciferase). Purple, red, and yellow lines denote Nbs 20, 21, and 89 with IC_{50} < 0.2 nM. Two different purifications of the pseudovirus were used. The average neutralization percentage was shown for each data point (n = 5 for Nbs 20 and 21; n = 2 for all other Nbs). (**D**) Neutralization potency of 14 neutralizing Nbs by SARS-CoV-2 plaque reduction neutralization test (PRNT). The average neutralization percentage was shown for each data point (n = 4 for Nbs 20, 21, and 89; n = 2 for other Nbs). (**E**) Summary table of pseudovirus and SARS-CoV-2 neutralization potencies of 18 Nbs. N/A, not tested. (**F**) SPR binding kinetics measurement for Nb21. Ka, acid dissociation constant; Kd, dissociation constant; K_D, equilibrium dissociation constant; RU, relative units.

shorter CDR3s (four amino acids shorter; P = 0.005) than other epitope binders (fig. S6I). Despite this, most of the selected Nbs potently inhibited the virus with an IC_{50} below 30 ng/ml (2 nM) (table S1).

To explore the molecular mechanisms that underlie the potent neutralization activities of epitope I Nbs, we determined a crystal structure of the RBD-Nb20 complex at a resolution of *3.3* Å by molecular replacement (materials and methods, table S3, and fig. S13). Most of the residues in the RBD (Asn^{334} to Gly^{526}) and in the entire Nb20, particularly those at the protein interaction interface, are well resolved.

There are two nearly identical copies of RBD-Nb20 complexes in one asymmetric unit, with a root mean square deviation of 0.277 Å over 287 Cα atoms. In the structure, all three CDRs of Nb20 interact with the RBD by binding to its large extended external loop with two short β strands (Fig. 3A) (*31*). Glu^{484} of the RBD forms hydrogen bonding and ionic interactions with the side chains of Arg^{31} (CDR1) and Tyr^{104} (CDR3) of Nb20, whereas Gln^{493} of the RBD forms hydrogen bonds with the main-chain carbonyl of Ala^{29} (CDR1) and the side chain of Arg^{97} (CDR3) of Nb20. These interactions constitute a major polar interaction network at the RBD and Nb20 interface. Arg^{31} of Nb20 also engages in a cation π interaction with the side chain of Phe^{490} of the RBD (Fig. 3B). In addition, Met^{55} from the CDR2 of Nb20 packs against residues Leu^{452}, Phe^{490}, and Leu^{492} of the RBD to form hydrophobic interactions at the interface. Another small patch of hydrophobic interactions is formed among residues Val^{483} of the RBD and Phe^{45} and Leu^{59} from the framework β sheet of Nb20 (Fig. 3C).

The binding mode of Nb20 to the RBD is distinct from those of other reported neutralizing Nbs, which generally recognize similar epitopes in the RBD external loop region (*32*–*34*) (fig. S8). The extensive hydrophobic and polar interactions (Fig. 3, B and C) between the RBD and Nb20 stem from the notable shape complementarity (Fig. 3D) between the CDRs and the external RBD loop, leading to ultrahigh affinity (~10 pM). On the basis of our crystal structure, we further modeled the structure of the best neutralizer Nb21 with the RBD (materials and methods). Only four residues vary between Nbs 20 and 21 (fig. S9A), all of which are on CDRs. Two substitutions are at the RBD binding interface. Ser^{52} and Met^{55} in the CDR2 of Nb20 are replaced by two asparagine residues (Asn^{52} and Asn^{55}) in Nb21. In our superimposed structure, Asn^{52} forms a new H bond with Asn^{450} of the RBD (fig. S9B). Although Asn^{55} does not engage in additional interactions with the RBD, it creates a salt bridge with the side chain of Arg^{31}, which stabilizes the polar interaction network among Arg^{31} and Tyr^{104} of Nb21 and Gln^{484} of the RBD (fig. S9B). All of those likely contribute to a slower off-rate of Nb21 (Fig. 1F and fig. S4A) and stronger neutralization potency. Structural comparison of RBD-Nb20 or RBD-Nb21 and RBD-hACE2 [Protein Data Bank (PDB) ID 6LZG] (*31*) clearly showed that the interfaces for Nb20 or Nb21 and hACE2 partially overlap (Fig. 3D and fig. S9C). Notably, the CDR1 and CDR3 of Nb20 or Nb21 would clash with the first helix of hACE2, the primary binding site for the RBD (fig. S9D).

To understand the antiviral efficacy of our Nbs, we superimposed RBD-Nb complexes on different spike conformations according to cryo–electron microscopy (cryo-EM) structures. We found that three copies of Nb20 or Nb21 can simultaneously bind all three RBDs in their "down" conformations (PDB ID 6VXX) (*4*) that correspond to the inactive spike (Fig. 4B). Our analysis indicates a potential mechanism by which Nbs 20 and 21 (epitope I) lock RBDs in their down conformation with ultrahigh affinity. Combined with the steric interference with hACE2 binding in the RBD open conformation (Fig. 4A), these mechanisms may explain the exceptional neutralization potencies of epitope I Nbs.

Other epitope binders do not fit into this inactive conformation without steric clashes and appear to use different neutralization strategies (Fig. 4C). For example, epitope II (Nb93) colocalizes with the hACE2 binding site and can bind the spike in the one RBD "up" conformation (Fig. 4D; PDB ID 6VSB) (*3*). This epitope may neutralize the virus by blocking the hACE2 binding site. Epitope III and IV Nbs can bind only when two or three RBDs are in their up conformations (PDB ID 6XCN) (*24*), in which the epitopes are exposed. In the all-RBDs-up conformation, three copies of Nbs can directly interact with the trimeric spike. Through RBD binding, epitope III (Nb34) can be accommodated on top of the trimer to lock the helices of S2 in the prefusion stage, possibly preventing their large conformational changes for membrane fusion (Fig. 4E). When superimposed onto the all-up conformation, epitope IV (Nb95) is proximal to the rigid N-terminal domain (NTD) of the trimer, presumably restricting the flexibility of the spike domains (Fig. 4F). Future high-resolution structural studies (e.g., by cryo-EM) of these Nbs

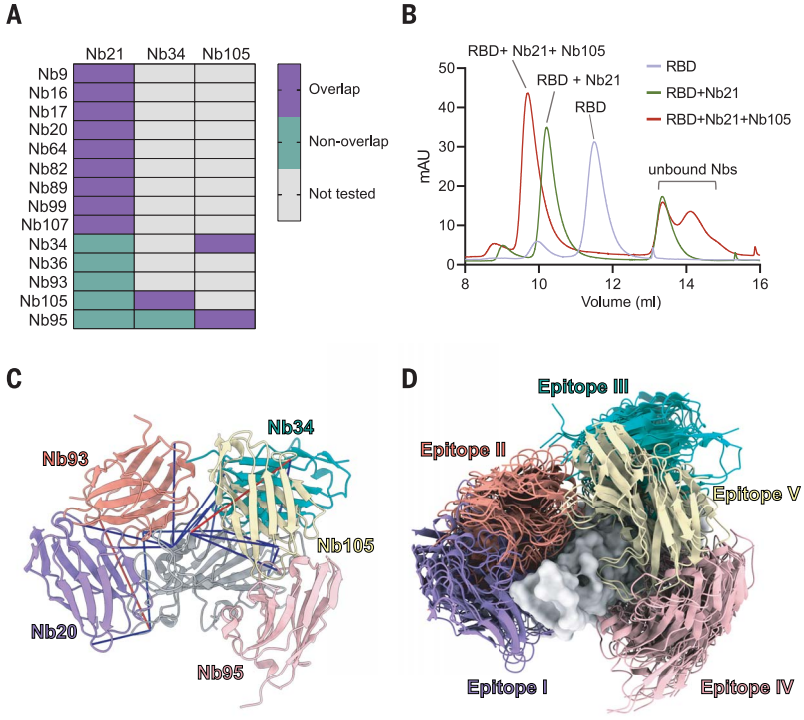

Fig. 2. Nb epitope mapping by integrative structural proteomics. (**A**) Summary of Nb epitopes on the basis of SEC analysis. Purple, Nbs that bind the same RBD epitope; green, Nbs of different epitopes; gray, not tested. (**B**) Representation of SEC profiling of the RBD, RBD-Nb21 complex, and RBD-Nb21-Nb105 complex. The *y* axis represents ultraviolet 280 nm absorbance units (mAu). (**C**) Cartoon model showing the localization of five Nbs that bind different epitopes: Nb20 (purple), Nb34 (green), Nb93 (dark pink), Nb105 (yellow), and Nb95 (light pink) in complex with the RBD (gray). Blue and red lines represent DSS cross-links shorter or longer than 28 Å, respectively. (**D**) Top-10-scoring cross-linking–based models for each Nb (cartoons) on top of the RBD surface.

in complex with the viral S protein will be needed to better understand the neutralization mechanisms.

Epitope mapping enabled us to bioengineer homo- and heterodimeric and homotrimeric Nbs. Homodimers and -trimers based on Nb20 or Nb21 were designed to increase the antiviral activities through avidity binding to the trimeric spike. Heterodimers pairing Nb21 with Nbs that bind a different epitope were designed to prevent viral escape. The homodimers and -trimers used flexible linker sequences of 25 (GS) or 31 (EK) amino acids (materials and methods). The heterodimers used flexible linkers of 12 amino acids.

Through a pseudovirus luciferase assay, we found up to ~30-fold improvement for the homotrimeric constructs of $Nb21_3$ (IC_{50} = 1.3 pM) and $Nb20_3$ (IC_{50} = 4.1 pM) compared with the respective monomeric form (Figs. 1, C and E, and 5, A and C). Similar results were obtained from the SARS-CoV-2 PRNT (Fig. 5, B and C, and fig. S11A). The improvements are likely greater than indicated by these values, as the measured values may reflect the assay's lower detection limits. For the heterodimeric constructs (i.e., Nb21-Nb34), we observed up to a fourfold increase of potency. The multivalent constructs retained similar physicochemical properties to those of the monomeric Nbs (including high solubility, yield, and thermostability) and remained intact (nonproteolyzed) under the neutralization assay condition (fig.

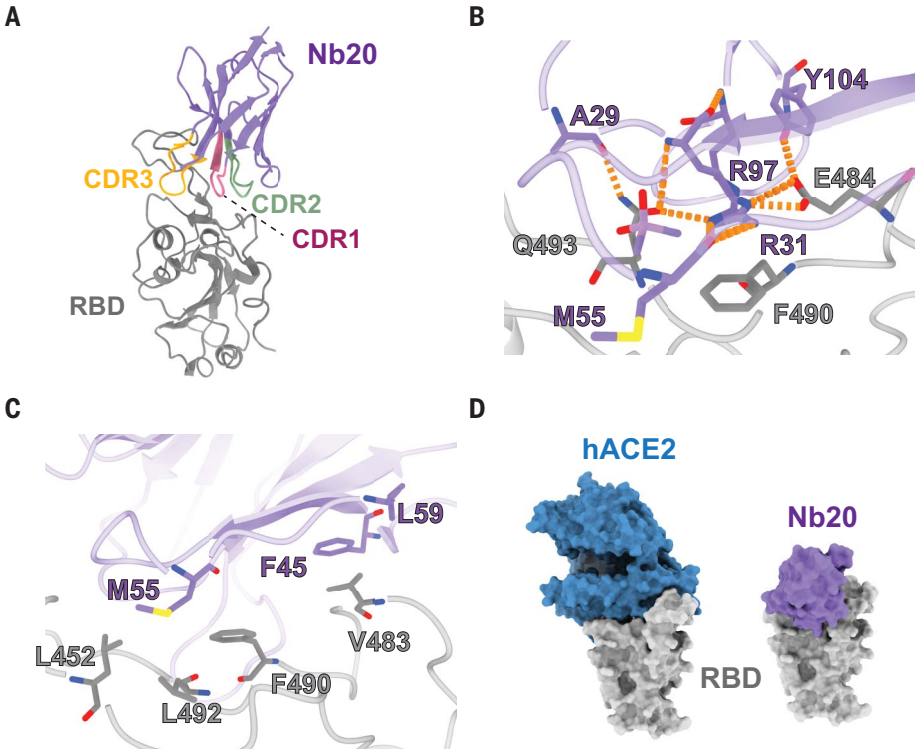

Fig. 3. Crystal structure analysis of an ultrahigh-affinity Nb in complex with the RBD. (**A**) Cartoon presentation of Nb20 in complex with the RBD. CDR1, -2, and -3 are in red, green, and orange, respectively. (**B**) Zoomed-in view of an extensive polar interaction network that centers on R35 of Nb20. (**C**) Zoomed-in view of hydrophobic interactions. (**D**) Surface presentation of the Nb20-RBD and hACE2-RBD complex (PDB ID 6M0J). Single-letter abbreviations for amino acid residues are as follows: A, Ala; E, Glu; F, Phe; L, Leu; M, Met; Q, Gln; R, Arg; V, Val.

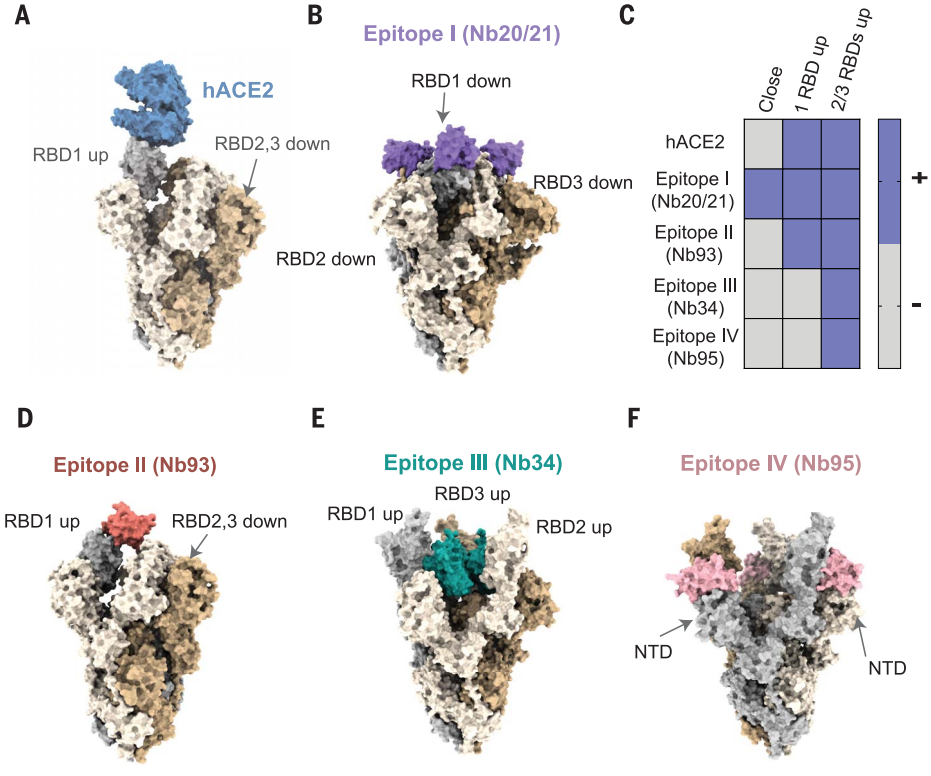

Fig. 4. Potential mechanisms of SARS-CoV-2 neutralization by Nbs. (**A**) hACE2 (blue) binding to spike trimer conformation (wheat, beige, and gray colors) with one RBD in the "up" conformation (PDB IDs 6VSB and 6LZG). (**B**) Nb20 (epitope I, purple) partially overlaps with the hACE2 binding site and can bind the closed spike conformation with all RBDs "down" (PDB ID 6VXX). (**C**) Summary of spike conformations accessible (+) to the Nbs of different epitopes. (**D**) Nb93 (epitope II, dark pink) partially overlaps with the hACE2 binding site and can bind to spike conformations with at least one RBD up (PDB ID 6VSB). (**E** and **F**) Nb34 (epitope III, green) and Nb95 (epitope IV, light pink) do not overlap with the hACE2 binding site and bind to spike conformations with at least two open RBDs (PDB ID 6XCN).

Fig. 5. Development of multivalent Nb cocktails for highly efficient SARS-CoV-2 neutralization.
(**A**) Pseudotyped SARS-CoV-2 neutralization assay of multivalent Nbs. The average neutralization percentage of each data point is shown (n = 2). ANTE-CoV2-Nab20T$_{GS/EK}$: homotrimeric Nb20 with the GS or EK linker; ANTE-CoV2-Nab21T$_{GS/EK}$: homotrimeric Nb21 with the GS or EK linker. (**B**) SARS-CoV-2 PRNT of monomeric and trimeric forms of Nbs 20 and 21. The average neutralization percentage of each data point is shown (n = 2 for the trimers; n = 4 for the monomers). (**C**) Summary table of the neutralization potency measurements of the multivalent Nbs. N/A, not tested. (**D**) Mapping mutations to localization of Nb epitopes on the RBD. The x axis corresponds to the RBD residue numbers (333 to 533). Rows in different colors represent different epitope residues. Epitope I: 351, 449 to 450, 452 to 453, 455 to 456, 470, 472, 483 to 486, and 488 to 496; epitope II: 403, 405 to 406, 408, 409, 413 to 417, 419 to 421, 424, 427, 455 to 461, 473 to 478, 487, 489, and 505; epitope III: 53, 355, 379 to 383, 392 to 393, 396, 412 to 413, 424 to 431, 460 to 466, and 514 to 520; epitope IV: 333 to 349, 351 to 359, 361, 394, 396 to 399, 464 to 466, 468, 510 to 511, and 516; epitope V: 353, 355 to 383, 387, 392 to 394, 396, 420, 426 to 431, 457, 459 to 468, 514, and 520.

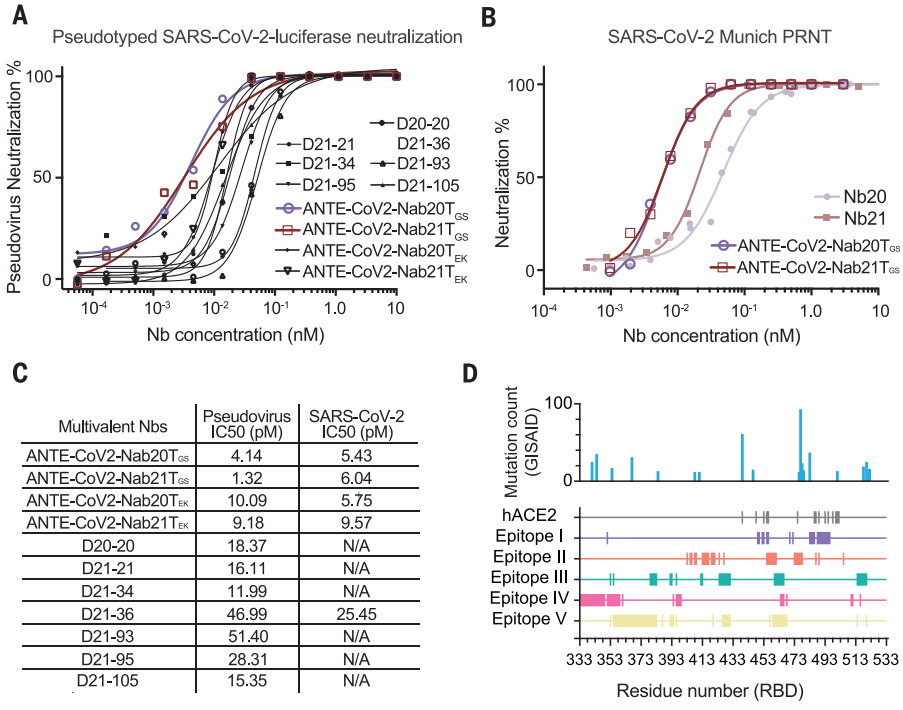

C

Multivalent Nbs	Pseudovirus IC50 (pM)	SARS-CoV-2 IC50 (pM)
ANTE-CoV2-Nab20T$_{GS}$	4.14	5.43
ANTE-CoV2-Nab21T$_{GS}$	1.32	6.04
ANTE-CoV2-Nab20T$_{EK}$	10.09	5.75
ANTE-CoV2-Nab21T$_{EK}$	9.18	9.57
D20-20	18.37	N/A
D21-21	16.11	N/A
D21-34	11.99	N/A
D21-36	46.99	25.45
D21-93	51.40	N/A
D21-95	28.31	N/A
D21-105	15.35	N/A

S10). They remained highly potent for pseudovirus neutralization after lyophilization and aerosolization (materials and methods and fig. S11, B to G), indicating the marked stability and potential flexibility of administration. Most of the RBD mutations observed in the Global Initiative on Sharing Avian Influenza Data (GISAID) (*35*) are very low in frequency (<0.0025), which may increase under Nb selection. Therefore, a cocktail consisting of ultrapotent, multivalent constructs that simultaneously bind a variety of epitopes with potentially different neutralization mechanisms will likely efficiently block virus mutational escape (Fig. 5E and fig. S12) (*9*, *36*–*38*).

In our study, in vivo antibody affinity maturation followed by advanced proteomics (*25*) enabled the rapid discovery of a diverse repertoire of high-affinity RBD Nbs, including an ultrapotent neutralizer with subpicomolar affinity, which is unusual for natural, single-domain antibody fragments. We demonstrated the simplicity and versatility of Nb bioengineering and the desirable physicochemical properties of the monomeric Nbs and their multivalent forms. To our knowledge, the multivalent constructs represent the most potent SARS-CoV-2 neutralizers to date. Flexible and efficient administration, such as inhalation, may further improve their antiviral efficacy while minimizing the dose, cost, and potential toxicity for clinical applications. The high sequence similarity between Nbs and human IgGs may restrain the immunogenicity (*39*). It is possible to fuse the antiviral Nbs with highly stable albumin-Nb constructs (*40*) to improve pharmacokinetics. These high-quality Nbs can also be applied as rapid and economic point-of-care diagnostics. We envision that the Nb technology described here will contribute to curbing the current pandemic and possibly a future event.

REFERENCES AND NOTES

1. N. Zhu *et al.*, *N. Engl. J. Med.* **382**, 727–733 (2020).
2. P. Zhou *et al.*, *Nature* **579**, 270–273 (2020).
3. D. Wrapp *et al.*, *Science* **367**, 1260–1263 (2020).
4. A. C. Walls *et al.*, *Cell* **181**, 281–292.e6 (2020).
5. Y. Cai *et al.*, *Science* **369**, 1586–1592 (2020).
6. X. Fan, D. Cao, L. Kong, X. Zhang, *Nat. Commun.* **11**, 3618 (2020).
7. Y. Cao *et al.*, *Cell* **182**, 73–84.e16 (2020).
8. D. F. Robbiani *et al.*, *Nature* **584**, 437–442 (2020).
9. J. Hansen *et al.*, *Science* **369**, 1010–1014 (2020).
10. L. Liu *et al.*, *Nature* **584**, 450–456 (2020).
11. P. J. M. Brouwer *et al.*, *Science* **369**, 643–650 (2020).
12. D. Wrapp *et al.*, *Cell* **181**, 1436–1441 (2020).
13. A. Z. Wec *et al.*, *Science* **369**, 731–736 (2020).
14. T. Zohar, G. Alter, *Nat. Rev. Immunol.* **20**, 392–394 (2020).
15. N. Eroshenko *et al.*, *Nat. Biotechnol.* **38**, 789–791 (2020).
16. S. Muyldermans, *Annu. Rev. Biochem.* **82**, 775–797 (2013).
17. P. Vanlandschoot *et al.*, *Antiviral Res.* **92**, 389–407 (2011).
18. L. Detalle *et al.*, *Antimicrob. Agents Chemother.* **60**, 6–13 (2015).
19. R. Konwarh, *Front. Immunol.* **11**, 1531 (2020).
20. T. F. Custódio *et al.*, bioRxiv 2020.06.23.165415 [Preprint]. 23 June 2020.
21. C. Liu *et al.*, bioRxiv 2020.03.02.972927 [Preprint]. 5 March 2020.
22. J. Gai *et al.*, bioRxiv 2020.08.09.242867 [Preprint]. 14 August 2020.
23. C. J. Bracken *et al.*, bioRxiv 2020.08.08.242511 [Preprint]. 10 August 2020.
24. C. O. Barnes *et al.*, *Cell* **182**, 828–842.e16 (2020).
25. Y. Xiang *et al.*, bioRxiv 2020.08.21.261917 [Preprint]. 23 August 2020.
26. W. B. Klimstra *et al.*, *J. Gen. Virol.* 10.1099/jgv.0.001481 (2020).
27. M. P. Rout, A. Sali, *Cell* **177**, 1384–1403 (2019).
28. C. Yu, L. Huang, *Anal. Chem.* **90**, 144–165 (2018).
29. A. Leitner, M. Faini, F. Stengel, R. Aebersold, *Trends Biochem. Sci.* **41**, 20–32 (2016).
30. B. T. Chait, M. Cadene, P. D. Olinares, M. P. Rout, Y. Shi, *J. Am. Soc. Mass Spectrom.* **27**, 952–965 (2016).
31. Q. Wang *et al.*, *Cell* **181**, 894–904.e9 (2020).
32. T. Li *et al.*, bioRxiv 2020.06.09.143438 [Preprint]. 24 September 2020.
33. J. D. Walter *et al.*, bioRxiv 2020.04.16.045419 [Preprint]. 16 May 2020.
34. J. Huo *et al.*, *Nat. Struct. Mol. Biol.* **27**, 846–854 (2020).
35. Y. Shu, J. McCauley, *Euro Surveill.* **22**, 30494 (2017).
36. A. Baum *et al.*, *Science* **369**, 1014–1018 (2020).
37. Y. Bar-On *et al.*, *Nat. Med.* **24**, 1701–1707 (2018).
38. M. Marovich, J. R. Mascola, M. S. Cohen, *JAMA* **324**, 131–132 (2020).
39. I. Jovčevska, S. Muyldermans, *BioDrugs* **34**, 11–26 (2020).
40. Z. Shen *et al.*, bioRxiv 2020.08.19.257725 [Preprint]. 20 August 2020.

ACKNOWLEDGMENTS

We thank the staff at the GM/CA of APS in the Argonne National Laboratory (USA) for their assistance with x-ray diffraction data collection. We thank the UPMC Genome Center for Illumina MiSeq, Z. Wei (Southern University of Science and Technology) for the help with crystal structure determination, and Y. Liu for critical reading of the manuscript. **Funding:** This work was supported by the University of Pittsburgh School of Medicine (Y.S.), a Clinical and Translational Science Institute (CTSI) pilot fund (Y.S.), NIH grant R35GM137905 (Y.S.), the University of Pittsburgh and the Center for Vaccine Research (W.P.D.), NIH grant R35GM128641 (C.Z.), ISF 1466/18 (D.S.-D.), and Israeli Ministry of Science and Technology (D.S.-D.). **Author contributions:** Y.S. and D.S.-D. conceived the study. Y.X. performed most of the experiments. S.N. performed the PRNT SARS-CoV-2 neutralization assay. Z.X. produced the multivalent Nbs and performed thermostability measurements. C.Z. determined the x-ray structure, with the help of H.L. Y.X., Y.S., D.S.-D., C.Z., Z.S., S.N., and W.P.D. analyzed the data. Y.S. supervised the study and drafted the manuscript. All authors edited the manuscript. **Competing interests:** Y.X. and Y.S. are co-inventors on a provisional patent filed by the University of Pittsburgh covering the Nbs described in this manuscript. **Data and materials availability:** The coordinates and structure factors for the SARS-CoV-2 RBD with Nb20 have been deposited in the Protein Data Bank under PDB ID 7JVB. The proteomics data

SUPPLEMENTARY MATERIALS

science.sciencemag.org/content/370/6523/1479/suppl/DC1
Materials and Methods
Figs. S1 to S13
Tables S1 to S4
References (*41*–*60*)
MDAR Reproducibility Checklist

View/request a protocol for this paper from *Bio-protocol*.

24 August 2020; accepted 28 October 2020
Published online 5 November 2020
10.1126/science.abe4747